



Interventional digital tomosynthesis from a standard fluoroscopy system using 2D–3D registration [☆]



Mazen Alhrishy ^{a,*}, Andreas Varnavas ^a, Tom Carrell ^b, Andrew King ^a, Graeme Penney ^a

^a Biomedical Engineering Dept., King's College London, King's Health Partners, London, UK

^b Vascular Surgery Dept., Guys & St Thomas' NHS Foundation Trust, King's Health Partners, London, UK

ARTICLE INFO

Article history:

Received 14 March 2014

Received in revised form 29 July 2014

Accepted 7 October 2014

Available online 16 October 2014

Keywords:

Interventional digital tomosynthesis

2D–3D image registration

Endovascular aneurysm repair

ABSTRACT

Interventional fluoroscopy provides guidance in a variety of minimally invasive procedures. However, three-dimensional (3D) clinically relevant information is projected onto a two-dimensional (2D) image which can make image interpretation difficult. Moreover, vasculature visualisation requires the use of iodinated contrast media which is nephrotoxic and is the primary cause of renal complications. In this article, we demonstrate how digital tomosynthesis slices can be produced on standard fluoroscopy equipment by registering the preoperative CT volume and the intraoperative fluoroscopy images using 2D–3D image registration. The proposed method automatically reconstructs patient-anatomy-specific slices and removes clutter resulting from bony anatomy. Such slices could provide additional intraoperative information which cannot be provided by the preoperative CT volume alone, such as the deformed aorta position offering improved guidance precision. Image acquisition would fit with interventional clinical workflow and would not require a high X-ray dose. Experiments are carried out using one phantom and four clinical datasets. Phantom results showed a 3351% contrast-to-noise improvement compared to standard fluoroscopy. Patient results showed our method enabled visualization of clinically relevant features: outline of the aorta, the aortic bifurcation and some aortic calcifications.

© 2014 Elsevier B.V. All rights reserved.

1. Introduction

Interventional fluoroscopy uses X-ray to provide guidance in a variety of minimally invasive procedures, such as vascular interventions. During such interventions, catheters, guide wires, or other interventional instruments are inserted into the patient's arteries and their movement is monitored in real-time on a set of display screens in the intervention room as seen in Fig. 1. The requirements for an interventional modality are different to imaging systems used for diagnosis. High frame rate to guide instruments and low radiation dose so repeated imaging is clinically acceptable are very important. In addition both image acquisition

and subsequent viewing of images should have minimal interruption to clinical work-flow.

Fluoroscopy screening uses low tube voltage to offer repeated low-dose real-time imaging of interventional devices and dense tissues such as bone. However, soft tissue anatomy, such as vasculature, cannot be imaged using fluoroscopy. Moreover, fluoroscopy images are projection images, i.e. 2D, which simply integrate all information along the beam path. This often results in clinically relevant information being obscured by over- or under-lying anatomy irrelevant to the procedure.

To visualise vasculature, angiography imaging is often employed. This uses an intravascular iodinated contrast medium and images with a higher radiation dose than standard screening fluoroscopy. To remove background structures from an angiography image, a reference image acquired before contrast injection can be subtracted from the subsequent angiography images, resulting in a digitally subtracted angiogram (DSA) showing only the enhanced vasculature. Contrast usage is routine during interventional procedures, but nevertheless, it must be administered sparingly as the contrast medium is nephrotoxic and can cause renal failure (McCullough, 2008). Contrast medium injection has become the third leading cause for hospital acquired renal failure (Seeliger et al., 2012).

[☆] The authors acknowledge financial support from King's Overseas Research Studentship (KORS), Guy's and St Thomas' Charity, and the department of health via the National Institute for Health Research (NIHR) comprehensive Biomedical Research Centre award to Guy's & St Thomas' NHS Foundation Trust in partnership with King's College London and King's College Hospital NHS Foundation Trust. Thanks also go to all clinical staff at St. Thomas' Hospital who aided this research.

* Corresponding author.

E-mail addresses: mazen.m.alhrishy@kcl.ac.uk (M. Alhrishy), andreas.varnavas@kcl.ac.uk (A. Varnavas), tom.carrell@kcl.ac.uk (T. Carrell), andrew.king@kcl.ac.uk (A. King), graeme.penney@kcl.ac.uk (G. Penney).

Limited angle tomography was the first medical sectional modality, but was largely superseded by CT after its invention in the 1970s. However, in the last decade digital tomosynthesis (DTS) has been increasingly used for diagnosis of breast lesions (Teertstra et al., 2010; Skaane et al., 2012) and pulmonary nodules in the chest (Dobbins et al., 2008; Dobbins and McAdams, 2009). For chest imaging, DTS is used as an alternative to CT as it offers substantial lower dose and cost and shorter acquisition time. Moreover, for breast imaging, DTS improved the detectability of lesions as it provides 3D information instead of the 2D projection images provided by the current gold-standard breast screening modality, i.e. mammography (Dobbins, 2009; Tingberg, 2010). Nevertheless, such diagnostic systems require dedicated equipment and suffer from the presence of background “clutter”, which comes from high contrast features outside the slice of interest (Levakhina et al., 2013).

In this article, we propose the use of DTS as an interventional modality which allows repeated low-dose acquisitions and results in minimal interruption to standard clinical work-flow. Our proposed use of DTS is not to reconstruct a 3D volume, as this would then require clinical input to scroll to the relevant slice. Instead we propose to automatically reconstruct the information lying on a clinically relevant section or slice of interest. This is then projected into the fluoroscopy image resulting in minimal interruption to the clinical work-flow.

By using the existing preoperative CT volume, and a 2D-3D registration algorithm (Penney et al., 2011), our proposed methods can:

- Reconstruct DTS slices using a standard fluoroscopy system.
- Automatically reconstruct patient-anatomy-specific DTS slices that display the most clinically relevant information.
- Automatically remove clutter resulting from bony anatomy.

Our primary clinical application is for DTS slices to provide information about the position of the aorta during endovascular aortic repair (EVAR). This often cannot be provided purely by the CT scan as aortic deformation occurs due to the rigid interventional instruments (Demirci et al., 2009; Carrell et al., 2010). DTS has the potential to provide information on the position of the aorta during

an intervention without the use of contrast agents. In addition it could be used to provide information to update a 2D-3D registration to account for intraoperative deformation.

Another imaging modality which is now available in most modern fluoroscopy suites is cone-beam CT (CBCT), which provides 3D imaging via semicircular rotation of the C-arm. However, the set-up time for CBCT (5 ~ 10 min) can cause a large interruption to clinical work-flow, especially if multiple acquisitions are required (Wallace et al., 2008). This is because the full 180° rotation required by CBCT needs accurate centreing (much more than for a small 40° sweep). Care also needs to be taken that anesthetic equipment will not be in the rotation path, and that the surgical sterile area will not be compromised. The 3D nature of CBCT images requires some interaction from interventionists to scan through 2D sections to find the clinically relevant information. Furthermore, repeated cone-beam CT involves a significant radiation dose (Bachar et al., 2007). For these reasons, cone-beam CT is not a natural interventional modality, and is unlikely to be used repeatedly during interventions to aid guidance.

In the following we firstly provide a brief overview of standard DTS slice reconstruction. We then explain how our novel methods work by using a preoperative CT volume and 2D-3D registration. Experiments are then described, and results presented using data from an abdominal phantom and four patient datasets.

2. Overview of standard digital tomosynthesis

Standard DTS slice reconstruction requires a set of 2D X-ray images to be acquired from a limited range of view directions. These are reconstructed into a sectional slice, commonly using the shift and add method (Dobbins and Godfrey, 2003). This method combines the images so that structures in the reconstruction plane line-up, and so appear in-focus, while structures outside the reconstruction plane are not aligned, and so are blurred-out. The shift and add method is illustrated in Fig. 2 where the five resulting projection images in Fig. 2(a) can be shifted and added so structures in either plane A or B appear in-focus as in Fig. 2(b).

In the following we describe the information needed for standard DTS slice reconstruction and the main effect which limits image quality: out-of-plane clutter.

2.1. Standard DTS required information and main limitation

To reconstruct a DTS slice through an imaged object (e.g. cylinder in Fig. 3(a)), the following spatial positions need to be known in the same coordinate system:

- I. Positions of source and detector when each 2D image was acquired.
- II. Reconstruction plane position.

Standard diagnostic DTS equipment calculates source and detector positions using mechanical tracking. This requires calibration to correct for the gravity-induced mechanical flex. When the flex is not reproducible, or not accurately corrected for during reconstruction, input images are misregistered which causes artifacts and reduces image quality (Jaffray et al., 2002). The magnitude of such flex increases with higher angulation and can reach up to ~14 mm at 45° (Orth et al., 2008).

In standard diagnostic DTS equipment, usually a number of parallel slices are reconstructed with spacing determined by the clinical application (e.g. ~1 mm for breast and ~5 mm for chest) (Dobbins, 2009). Therefore, prior to reconstruction, it is not possible to define a reconstruction plane to image specific regions of the

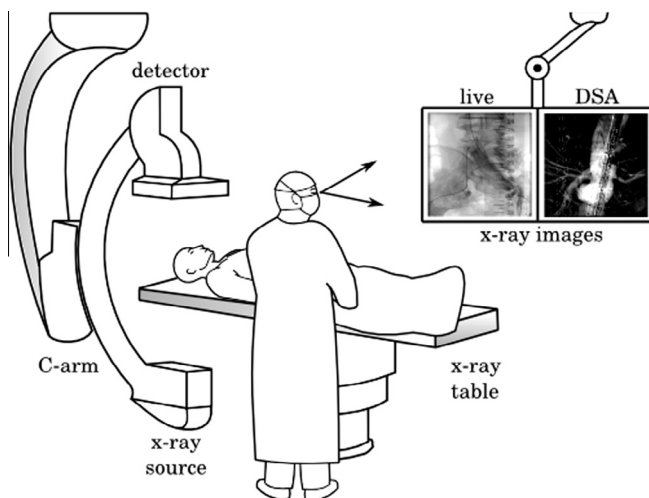


Fig. 1. Standard interventional fluoroscopy setting. The fluoroscopy provides live 2D images with high contrast for interventional instruments and bony anatomy. The C-arm is positioned (rotated and translated) to provide the most appropriate view using the 2D images. This view will change many times during the course of the operation. The live 2D image, plus useful previously acquired 2D images, are displayed so the surgeon can easily see them while manipulating the interventional instruments.

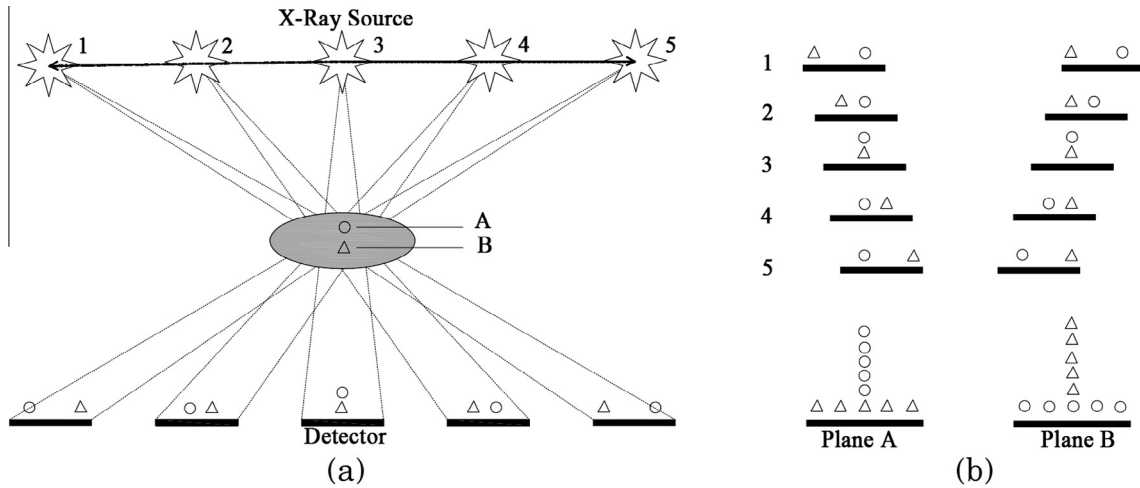


Fig. 2. The shift and add reconstruction method. (a) the relative projected locations of the circle and triangle change as the X-ray tube moves. (b) images can be shifted and added so structures in either plane A or B are in-focus while structures in other planes are blurred-out.

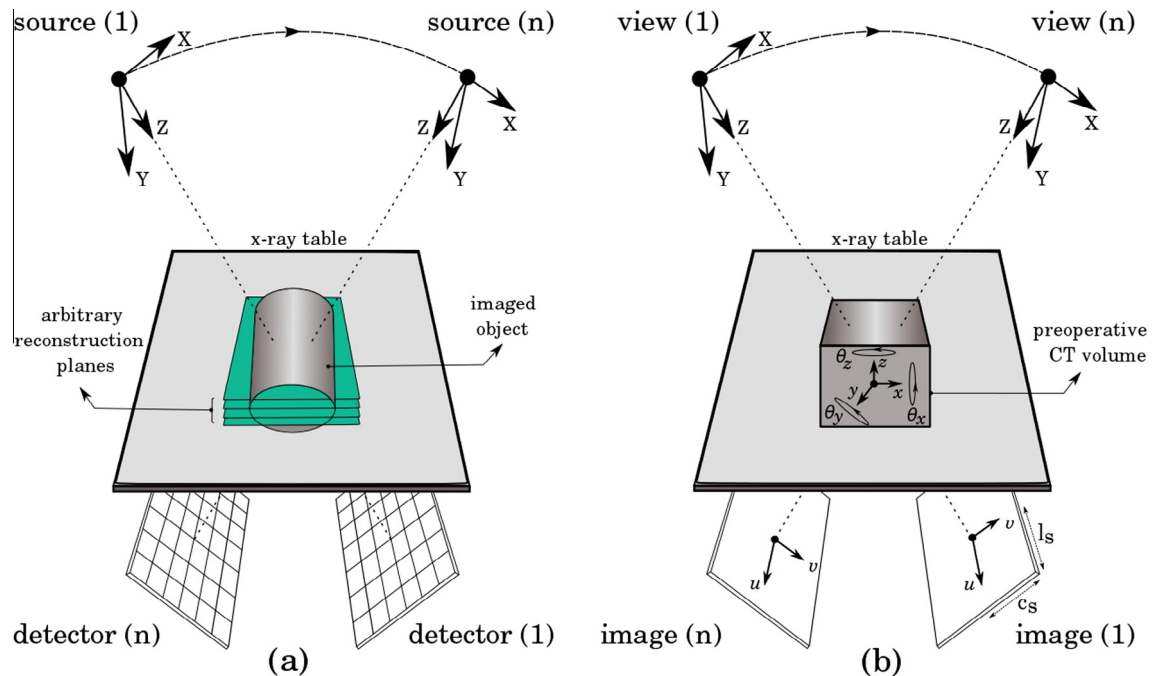


Fig. 3. The X-ray gantry moves around the object to acquire n projections. (a) Four coronal reconstruction planes are arbitrarily defined inside the imaged object according to the imaging device. (b) A preoperative CT volume is registered with the intraoperative images using a 2D-3D registration algorithm, this enables the position of the X-ray source and detector to be determined relative to the CT coordinate system.

patient's anatomy. An example is given in Fig. 3(a) where 4 arbitrary reconstruction planes are shown with equal spacing.

DTS attempts to blur-out all structures outside the reconstruction plane, but because of the limited data acquisition, clutter from high contrast structures above and below the reconstruction plane remain. This can obscure details in the reconstruction plane and lowers their contrast. A number of methods have been proposed to reduce the effect of clutter (Dobbins and Godfrey, 2003), but this remains one of the main problems of DTS (Gang et al., 2010).

To our knowledge, DTS slices have not yet been reconstructed using standard fluoroscopy systems. Recently, however, a 3D DTS prototype system has been proposed for intraoperative guidance of head and neck surgery (Bachar et al., 2007, 2009; Siewerdsen et al., 2007). The prototype is based on a mobile isocentric C-arm, modified for DTS acquisition. The limited DTS arc (e.g.

$20^\circ \sim 90^\circ$) enabled a short acquisition time and low radiation dose causing a minimal interruption to the surgical work-flow (Bachar et al., 2007). However, apart from being modified for intraoperative use, the prototype still employs the same technique as diagnostic DTS systems and suffers from the same main drawback: out-of-plane clutter.

3. Materials and methods

A large number of 2D-3D registration algorithms have been proposed in the literature for image-guided interventions (Markelj et al., 2012). In this section we give an overview of the specific 2D-3D registration algorithm we used (Penney et al., 2011), and detail how this registration algorithm enables

patient-anatomy-specific DTS reconstruction, with greatly reduced out-of-plane clutter, using images from a standard fluoroscopy system. The section begins by defining the coordinate systems used.

3.1. Coordinate systems definition

Three coordinate systems are used through-out this paper:

1. \mathbf{X}_{3D} : the 3D X-ray fluoroscopy set coordinate system. This defines 3D positions with respect to the X-ray source and detector. Coordinates in \mathbf{X}_{3D} are defined with the capital letters (X, Y, Z) .
2. \mathbf{CT}_{3D} : the 3D preoperative CT scan coordinate system. This defines 3D positions in the preoperative CT scan. Coordinates in \mathbf{CT}_{3D} are defined with the small letters (x, y, z) .
3. \mathbf{I}_{2D} : the 2D X-ray image coordinate system. This defines 2D positions in the X-ray image. Coordinates in \mathbf{I}_{2D} are defined by (u, v) .

3.2. Overview of the 2D-3D registration algorithm

Our interventional DTS method uses an established intensity-based 2D-3D registration algorithm (Penney et al., 1998, 2011), which is currently in use at St Thomas' hospital (London, UK) for elective EVAR cases. The algorithm is currently used to align the preoperative CT scan with the fluoroscopy system coordinates to aid guidance during interventions.

The algorithm generates digitally reconstructed radiographs (DRRs) by casting rays through an automatically segmented vertebra from the preoperative CT, and integrating voxel values above a threshold (200 HU) along each ray. Therefore, DRR intensities only include voxel values from vertebral bone. DRRs are then compared with the intraoperative fluoroscopy images using a gradient difference similarity measure (Penney et al., 1998).

Fig. 3(b) shows the ten degrees of freedom involved in a perspective projection transformation: $W = (c_s, l_s, k_1, k_2, \theta_x, \theta_y, \theta_z, X, Y, Z)$. c_s and l_s are the 2D positions on the imaging plane where the normal to the imaging plane goes through the X-ray source. k_1 and k_2 are the focal length (source to image distance) divided by the 2D image pixel sizes. θ_x, θ_y , and θ_z represent the orientation, and X, Y , and Z represent the position of the CT coordinate system, \mathbf{CT}_{3D} , with respect to the fluoroscopy set coordinate system, \mathbf{X}_{3D} .

These ten parameters, W , can be combined to produce a projection transformation matrix $M(W)$, which is the product of a 3×4 perspective matrix $P(c_s, l_s, k_1, k_2)$, a 4×4 rotational matrix $R(\theta_x, \theta_y, \theta_z)$, and a 4×4 translation matrix $T(X, Y, Z)$, as shown in Eq. (1). Matrix $M(W)$ relates positions (represented as homogeneous coordinates) in the CT coordinate system, \mathbf{CT}_{3D} , and the 2D image coordinate system, \mathbf{I}_{2D} , as shown in Eq. (2), where λ is a scaling factor. Matrix $M(W)$ can be used to project a 3D point in \mathbf{CT}_{3D} to a 2D point in \mathbf{I}_{2D} , or to transform a 2D point in \mathbf{I}_{2D} to a 3D line in \mathbf{CT}_{3D} .

$$M(W) = P(c_s, l_s, k_1, k_2)R(\theta_x, \theta_y, \theta_z)T(X, Y, Z) \quad (1)$$

$$M(W)(x, y, z, 1)^T = \lambda(u, v, 1)^T \quad (2)$$

3.3. Using the 2D-3D registration algorithm to facilitate enhanced dts using a standard fluoroscopy system

The novelty of this paper lies in the use of the aforementioned 2D-3D registration to facilitate improved DTS reconstruction using standard hardware, on patient-anatomy-specific surfaces and with reduced clutter.

Fig. 4 shows the three ways in which the 2D-3D registration algorithm both enables and improves DTS. This begins at the top with the input images: a small angle C-arm sweep (Fig. 4(a)) to produce a set of intraoperative fluoroscopy images: I_1, \dots, I_n (Fig. 4(b)), and a preoperative CT scan (Fig. 4(c)). These images are input into the 2D-3D registration algorithm which calculates the 2D-3D transformations, M_i , between the CT scan and each of the n fluoroscopy images i.e.

$$M_i(x, y, z, 1)^T = \lambda(u, v, 1)^T_i, i = 1, \dots, n \quad (3)$$

The registrations provide the necessary information to carry out DTS (as was described for standard DTS in Section 2.1) and enables us to greatly reduce clutter from bone. This is illustrated by the three boxes showing the subsequent stages to the 2D-3D registration in Fig. 4e Roman numerals labelling each box correspond to the descriptions below:

- I. Calculate view positions: The transformations M_i can be used to determine the relative positions between all the input 2D image views. The relative motion of \mathbf{X}_{3D} with respect to \mathbf{CT}_{3D} between view positions i_2 and i_1 can be described by the transformation $(R_2 T_2)^{-1} R_1 T_1$.
- II. Position reconstruction surface: A patient-anatomy-specific plane can be preoperatively defined inside the CT scan. The transformations M_i can position this plane with respect to any of the fluoroscopy images, enabling reconstruction to occur on a patient-anatomy-specific plane. In addition, we propose the use of curved patient-anatomy-specific reconstruction surfaces. It is rare that structures of clinical interest lie on flat planes. Our aim in interventional DTS is to produce images with enhanced clinically relevant structures. As shown in Fig. 5, if the structure of clinical interest is the aorta, then only approximately half of its length could be included in a flat reconstruction plane (Fig. 5(a) and (b)), whereas the use of a curved surface allows reconstruction of the entire length of the aorta (Fig. 5(c) and (d)).
- III. Remove bones: high attenuation bony features are the largest cause of out-of-plane clutter which will greatly reduce DTS image quality. However, because our method accurately registers vertebra between the CT and fluoroscopy image we are able to subtract fluoroscopy intensities arising due to the vertebra prior to DTS image reconstruction. This has the potential to greatly reduce the effect of clutter from out-of-plane vertebra features. Our method uses the DRR produced from a vertebra at the current registration position. Note that because the vertebrae are segmented from the CT scan (by defining a rough bounding box and only integrating Hounsfield values above 200) the DRR should contain only information from the vertebra (see Fig. 6(a)). These DRR vertebra intensities have an approximate linear relationship to the fluoroscopy image intensities from the vertebra (see Fig. 6(b)). The Pattern Intensity similarity measure (Weese et al., 1997) is used to calculate the correct scaling factor s . This requires production of a difference image I_{diff} as described by Eq. (4) where I_{fluoro} and I_{DRR} are the fluoroscopy and DRR image intensities respectively.

$$I_{diff}(u, v) = I_{fluoro}(u, v) - s \times I_{DRR}(u, v) \quad (4)$$

The optimal value for s is the value which maximises $P_{r,\sigma}(s)$ as described in Eqs. (5) and (6) where the values of σ and r were 10 and 3 respectively, as per Weese et al. (1997). High Pattern Intensity values are achieved when I_{diff} has few features. This will occur when the value of s has been found which removes as many of the vertebral features as possible. An example is shown in Fig. 6(c) where

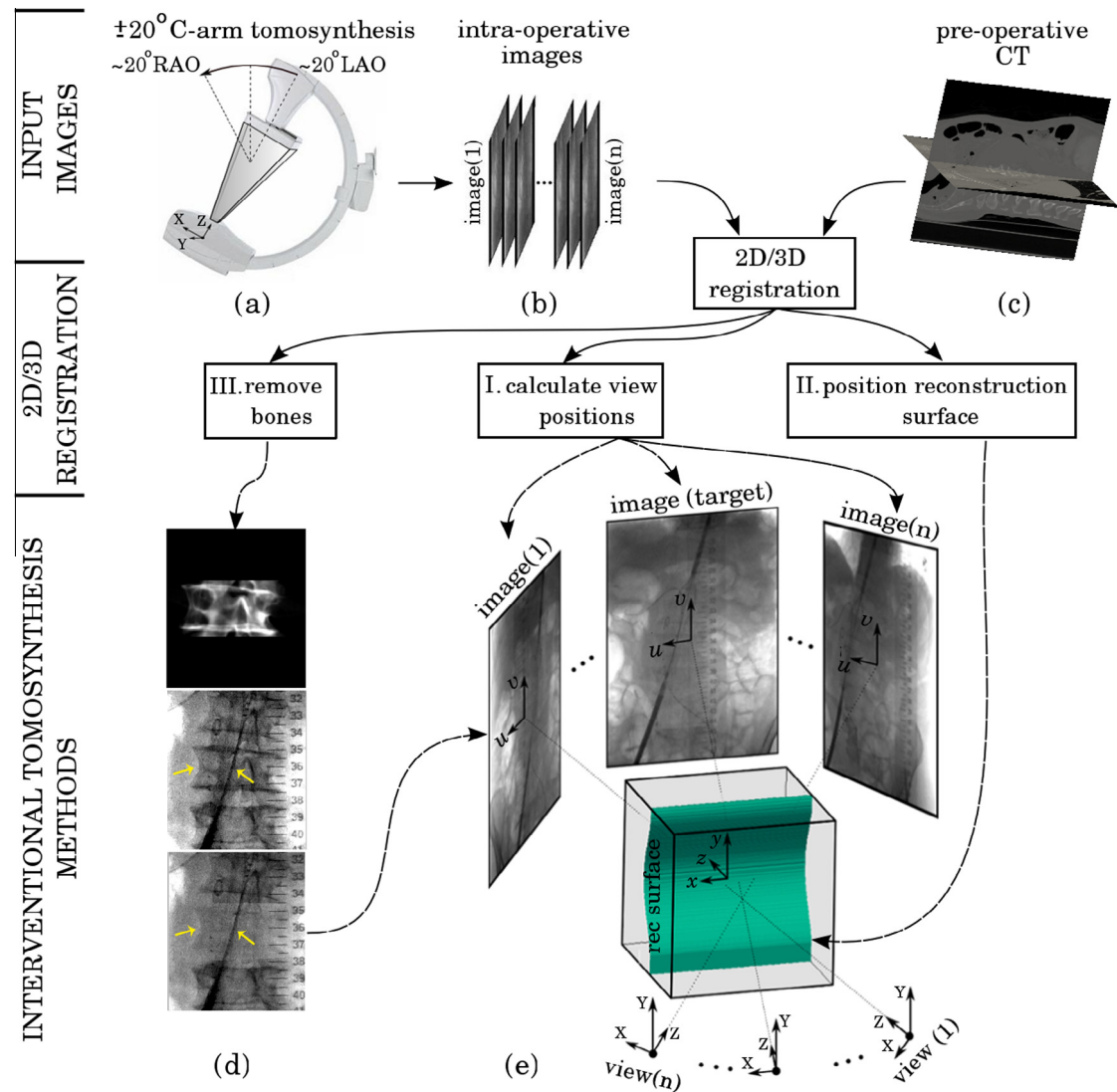


Fig. 4. Flow diagram showing how the 2D-3D registration algorithm enables DTS. Top shows input images: intraoperative fluoroscopy images (a,b) and preoperative CT (c). Middle and bottom shows the 2D-3D registration which enables bone removal (d), and calculation of view directions and positioning of curved patient-anatomy-specific reconstruction surface (e).

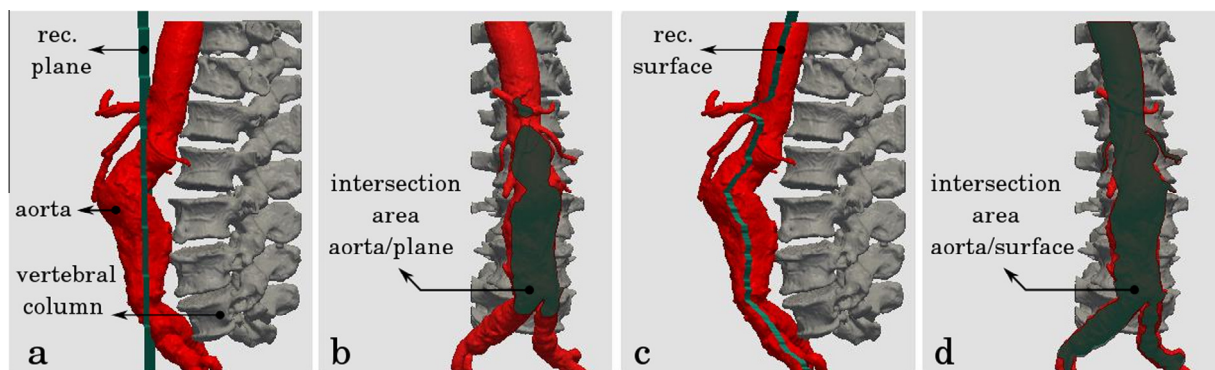


Fig. 5. Illustration of the advantage of using a curved surface over flat plane for DTS where the aorta is the feature of clinical interest: (a,c) sagittal views showing (a) flat reconstruction plane intersecting the aorta and (c) curved reconstruction surface along the aortic centreline; (b,d) anterior views showing (b) flat plane only intersects with roughly half of the aorta whereas (d) curved surface can intersect (and therefore can reconstruct) the entire aorta.

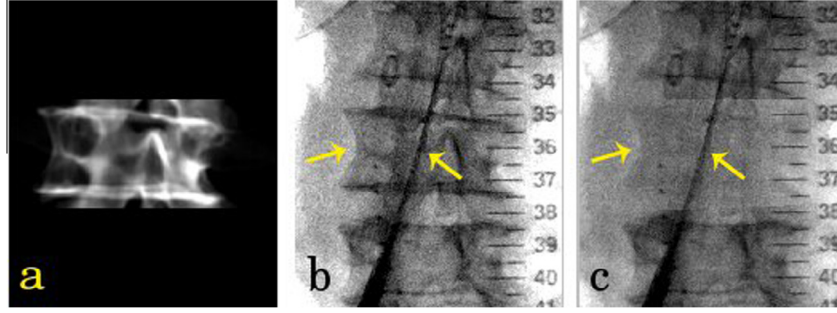


Fig. 6. (a) DRR of the L3 vertebra (bony feature), (b) fluoroscopy image before and (c) after “deboning” L3. Arrows indicate L3 and catheter.

features from the L3 can be seen to have been almost completely removed, leaving non-vertebra features which will be reconstructed using the DTS process.

$$P_{r,\sigma}(s) = \sum_{u,v} \sum_{d^2 \leq r^2} \frac{\sigma^2}{\sigma^2 + (I_{diff}(u,v) - I_{diff}(i,j))^2} \quad (5)$$

$$d^2 = (u - i)^2 + (v - j)^2 \quad (6)$$

Prior to DTS image reconstruction, all the vertebra from each of the fluoroscopy images are subtracted using the process described above. DTS image reconstruction is then carried out using these “deboned” fluoroscopy images.

3.4. Interventional DTS reconstruction process

In the previous section we explained how the 2D-3D registration can facilitate DTS on a standard fluoroscopy system. In this

section, the detailed reconstruction process of interventional DTS is given step by step as shown in Fig. 7, where the Roman numerals in the figure correspond to the following steps:

- I. Segmenting a reconstruction surface (S_{rec}) from the preoperative CT. The surface should be chosen to contain structures of clinical interest to be enhanced.
- II. Selecting a target image (I_T). This image is the fluoroscopy view the clinicians wish to use to guide their instruments. It could be chosen from one of the sweep images, or, after the sweep, the C-arm could be rotated back to the chosen clinical view and a single image is acquired and would be designated as the target image (I_T). In this latter case I_T should be contained within the range of the sweep images.
- III. Carrying out 2D-3D registration between the CT scan and each input fluoroscopy image using the 2D-3D registration algorithm as described in Section 3.3. This allows spatial

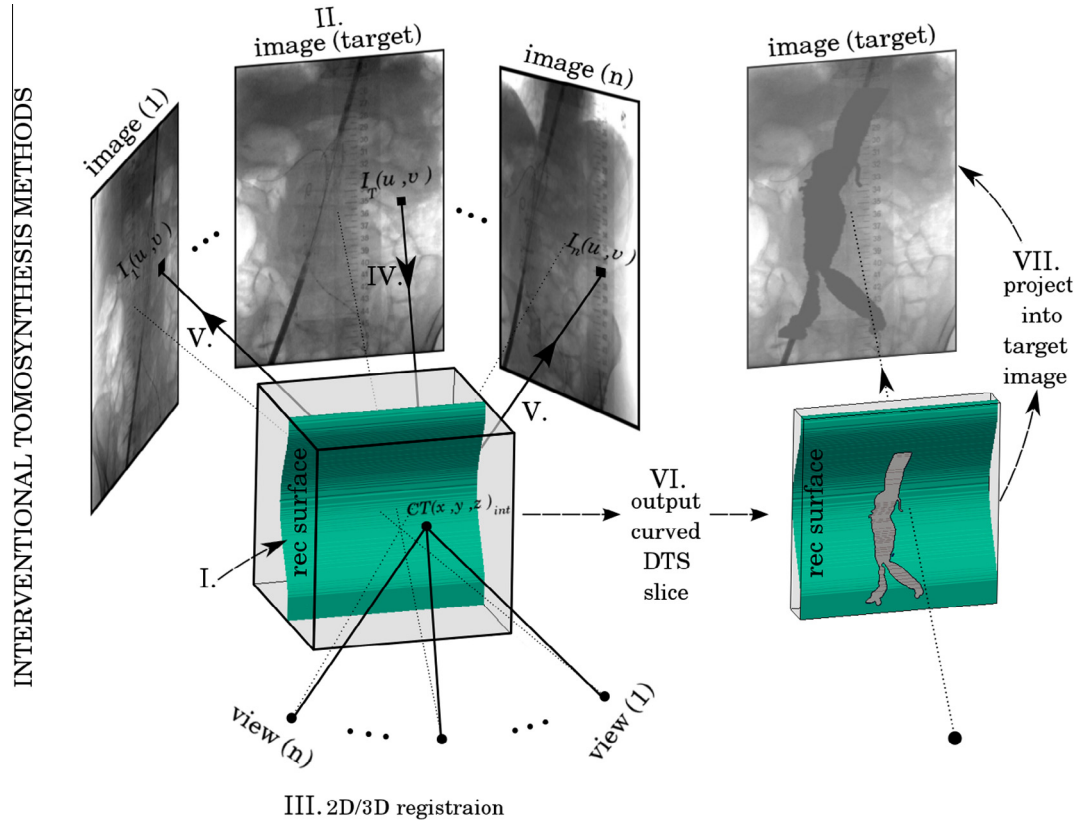


Fig. 7. Interventional DTS reconstruction process shown for one of the target image pixels: $I_T(u,v)$. A ray is back projected from $I_T(u,v)$ into the reconstruction surface using M_T . The 3D interception position $CT(x,y,z)_{int}$ is then projected into each fluoroscopy image in turn using the transformations M_i . The intensity at each 2D interception position $I_1(u,v), \dots, I_n(u,v)$ is mapped back onto the reconstruction surface at $CT(x,y,z)_{int}$. The process is repeated for all target image pixels and the intensity values from all fluoroscopy images at each 3D interception position are averaged to calculate the intensity value of the curved DTS slice. These intensity values, which contain additional clinical information, are then projected into the target fluoroscopy image to aid guidance.

positioning of the fluoroscopy images in relation to the segmented CT reconstruction surface (Section 3.3. I&II), and deboning the fluoroscopy images prior to reconstruction (Section 3.3. III).

- IV. Back projecting rays from the target image pixels $I_T(u, v)$ using M_T , and calculating the 3D positions in \mathbf{CT}_{3D} where the rays intercept the reconstruction surface $\mathbf{CT}(x, y, z)_{int}$. This is denoted as in Eq. (7), where \mathcal{F}_T calculates the interception of a line projected from the 2D target image I_T with the 3D reconstruction surface S_{rec} . Function \mathcal{F}_T will take on different forms depending upon how the surface S_{rec} is defined. An analytic solution exists if S_{rec} is a simple surface. We use an iterative method to allow a wide range of possible surfaces to be used.
- $$\mathcal{F}_T(u, v, M_T, S_{rec}) = (x, y, z, 1)_{int}^T \quad (7)$$
- V. Projecting rays from the 3D interception positions to each of the other fluoroscopy images in turn to acquire the 2D interception position in \mathbf{I}_{2D} (i.e. $I_1(u, v), \dots, I_n(u, v)$). This is done using transformations M_i , i.e., $M_i(x, y, z, 1)_{int}^T = \lambda(u, v, 1)_i^T$.
 - VI. The intensity at each 2D position in the target image is mapped back onto the patient-anatomy-specific reconstruction surface at the corresponding 3D interception position. Then, the intensity values from all fluoroscopy images at each 3D interception position are averaged to produce a curved patient-anatomy-specific DTS slice.
 - VII. Finally, in order to allow effective use of this new information, the reconstructed slice is projected onto the target image being used to guide the operation. This automatically produces an enhanced fluoroscopy image which shows additional information of the clinical features of interest in the field of view the clinicians using. This can be expressed as in Eq. (8):

$$I_{Tomo}(u, v) = \frac{1}{n} \sum_{i=1}^n I_i(M_i(\mathcal{F}_T(u, v, M_T, S_{rec}))) \quad (8)$$

4. Data and experiments

Experiments were carried out using data from an abdominal spine phantom and from four patients who underwent endovascular aortic repair of an abdominal aortic aneurysm. The patient data was processed offline, i.e. not during procedure, and was approved by the national research ethics committee (09/H0707/64) with informed patient consent. No attempt was made to select particular patient cases based on image quality or amount of aortic deformation.

Each data set had a preoperative CT scan, acquired on a variety of machines depending on the referring hospital. The phantom and first three patient fluoroscopy data sets were acquired on a Siemens FP20 system, as the operations moved operating theatre the fourth patient data set was acquired on a Philips Allura Xper FD20 system. Intraoperative low dose screening images were acquired during the procedure by rotating the C-arm $\sim 20^\circ$ right/left anterior oblique (RAO/LAO) with a frame rate of 30 fps (phantom and first 3 patient datasets) and 15 fps (4th patient dataset). The acquired screening images were resampled to obtain one image per one degree of rotation, i.e. ~ 40 images.

DTS slice reconstruction, as described in Section 3.4, was carried out for each data set to reconstruct two interventional DTS slices: the first using the ~ 40 standard fluoroscopy images, and the second using the ~ 40 “debonded” fluoroscopy images.

4.1. Phantom experiment

The phantom used consisted of a pelvis and lumbar vertebrae encased in acrylic resin as shown in Fig. 8(a) and (b). A CT scan of the phantom was acquired with a voxel size of $1.094 \times 1.094 \times 1.487 \text{ mm}^3$. Two phantom experiments were carried out: the first to investigate the ability of DTS to enhance instruments and features such as calcium in the aortic wall; the second to investigate the ability of DTS to enhance lower contrast features i.e. to detect the outline of the aorta. Prior to fluoroscopy acquisition, for the first experiment, the following was attached to the anterior surface of the phantom: a catheter and three pieces of synthetic rubber compound (Blu-Tack) to represent calcium in the aortic wall, as seen in Fig. 8(a). For the second experiment a thin layer of synthetic rubber compound in the shape of an abdominal aortic aneurysm was placed on the anterior surface of the phantom in an anatomically realistic superior-inferior position, as seen in Fig. 8(b). For both experiments the anterior surface of the CT volume illustrated in Fig. 8(c) was used for the reconstruction surface S_{rec} .

To illustrate the advantage of using a curved surface over a flat plane for reconstruction, we also use a flat plane as our reconstruction surface, S_{rec} . As shown in Fig. 8(d) the flat plane only intersects part of the anterior surface of the phantom.

4.2. Experiment with patient data

Each patient's standard diagnostic CT scan was used. These had voxel sizes which ranged from $0.683 \times 0.683 \times 0.7 \text{ mm}^3$ to $0.974 \times 0.974 \times 1 \text{ mm}^3$.

For each patient, the aorta was segmented using a semi-automatic method in ITK-SNAP (Yushkevich et al., 2006). The

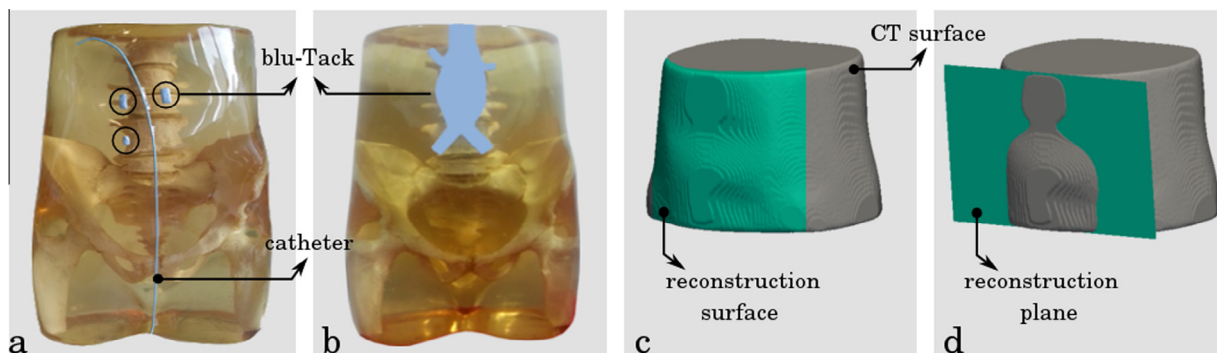


Fig. 8. (a,b) An anterior view of the used phantom with: (a) a catheter and 3 pieces of synthetic rubber compound (Blu-Tack) to represent calcium, and (b) one piece of synthetic rubber compound in the shape of an aortic aneurysm. (c,d) A 3D rendering of the CT surface with: (c) a reconstruction surface including the CT anterior surface, and (d) a reconstruction plane intersecting part of the CT anterior surface.

reconstruction surface was defined to be the surface which was perpendicular to the sagittal plane and which went through the centres of gravity of the segmented aorta in each axial slice. An example of such a reconstruction surface can be seen in Fig. 5 (c) and (d). This surface was chosen to enhance features of interest such as the aortic walls and calcium if present.

4.3. Validation experiments

For each experiment both standard DTS and deboned DTS slices were produced. These were both reconstructed using a sweep of ~ 40 fluoroscopy images. For comparison with images taken from a single view position the following two images were used:

1. The target image (I_T).
2. An image which required an equivalent amount of radiation as DTS, but was acquired from a single view point (i.e. no rotation). For the phantom experiments a specific set of images were acquired for this purpose. For the patient experiments a set of fluoroscopy images acquired as part of the routine intervention, at a time point close to when the DTS sweep was taken, were used. In both cases ~ 40 images were saved and averaged to produce a high contrast image (I_{HC}).

For the phantom data set, contrast-to-noise ratios (CNR) were calculated using profile lines (PL) through the synthetic calcium. CNR was calculated as $(\bar{I}_{FG} - \bar{I}_{BG})/\sigma_{BG}$, where \bar{I}_{FG} and \bar{I}_{BG} were the mean intensities of automatically delineated foreground (i.e. features of interest) and background profile line regions respectively, and σ_{BG} was the standard deviation of background intensities. The foreground and background regions were determined using the full width half maximum of the profile lines in the deboned DTS slice, and three calculations were made for each profile line. One directly on the profile line and two others with the profile line shifted vertically by ± 3 pixels. Averaging these CNR values increased the consistency of the CNRs.

For the patient data sets features enhanced by the DTS process were visually compared with the validation images, I_T and I_{HC} , and also with features overlaid from the CT scan. Two types of CT

feature were overlaid, the surface of the aorta, and aortic calcification. The overlay was initially achieved using the transformation provided by the 2D-3D registration algorithm (i.e. M_T). However, due to intraoperative deformation of the aorta (caused by the stiff interventional instruments), a manual adjustment process (in-plane translation) was required to accurately match the overlay with the DTS features. This illustrates one possible use of DTS images: to provide additional intraoperative information on the position of soft tissue structures to update a rigid-body registration.

5. Results

For each data set we show: (a) the target image (I_T), (b) the high contrast image (I_{HC}), (c) the reconstructed slice (DTS), and (d) the reconstructed slice after deboning, i.e. deboned DTS (DDTS).

5.1. Phantom results

Fig. 9 shows the phantom results using the reconstruction surface illustrated in Fig. 8(c). Results for the first experiment (catheter and synthetic calcium) are shown in the top row. The high contrast catheter can be seen in all these images. The low contrast synthetic calcium cannot be clearly distinguished from the overlying vertebrae in I_T (a) nor I_{HC} (b), whereas the synthetic calcium is clearly visible in both the DTS (c) and DDTS (d) images. Similar results are observed for the second experiment (aneurysm-shaped synthetic rubber compound) shown in the bottom row. The outline of the synthetic aorta is not visible in I_T (a) nor I_{HC} (b), but can be clearly seen in the DTS (c) and DDTS (d) images. The effect of the “deboning” process can clearly be seen in the results from both experiments by comparing the DTS (c) and DDTS (d) results. The horizontal bands in (c) are “clutter” caused by the high contrast vertebra edges, these are almost totally removed by the deboning process, as shown in the DDTS results (d).

Table 1 lists CNR results, and percentage improvement in CNR compared to I_T , calculated on PLs shown in Fig. 9(a) (top row) which are through synthetic calcium. An average improvement of

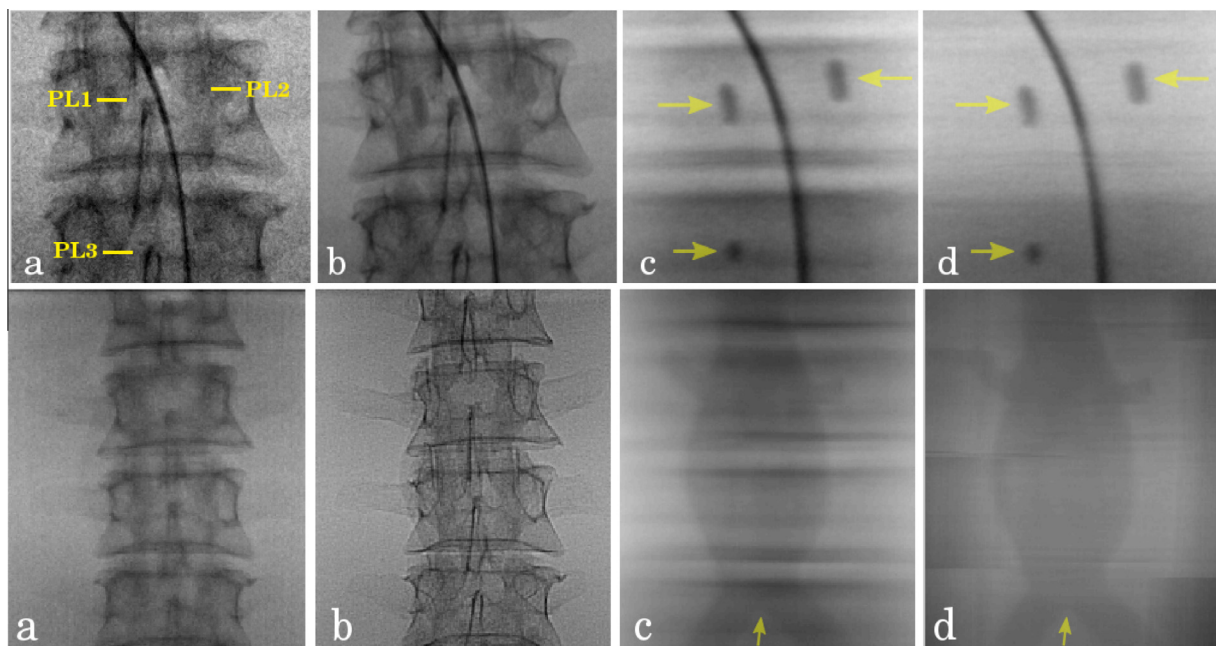


Fig. 9. Phantom results for the first experiment (top) and the second experiment (bottom): (a) I_T with profile lines positions, (b) I_{HC} , (c) DTS and (d) DDTS. Arrows indicate synthetic calcium (top) and aortic bifurcation (bottom).

Table 1

Calculated CNR, with improvement compared to I_T in brackets, for the three PLs shown in Fig. 9. Average improvement across the three PLs for each image is shown in bold text.

	I_T (a)	I_{HC} (b)	DTS (c)	DDTS (d)
PL1:CNR(imp.)	0.19 (–%)	0.78 (318%)	5.33 (2754%)	5.45 (2818%)
PL2:CNR(imp.)	0.11 (–%)	0.22 (98%)	3.43 (2907%)	5.53 (4750%)
PL3:CNR(imp.)	0.19 (–%)	0.57 (191%)	4.59 (2243%)	5.06 (2485%)
Average Imp.	–	202%	2635 %	3351%

Table 2

Calculated CNR using PLs 1,2 and 3 through synthetic calcium in the two reconstructed DDTS using a curved surface (Fig. 10(a)) and a flat plane (Fig. 10(b)), with the shortest distance from the centre of gravity of each piece of synthetic calcium to the flat plane in mm.

	CNR: curved surface (a)	CNR: flat plane (b)	Distance (mm)
PL1	5.45	5.31 (–2%)	1.09
PL2	5.52	5.91 (7%)	1.09
PL3	5.06	2.93 (–42%)	9.85

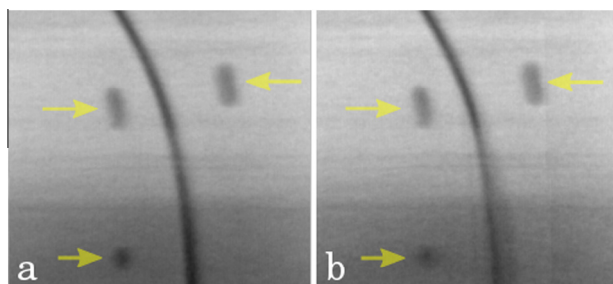


Fig. 10. Phantom results to show the advantage of using a curved surface over a flat plane. Two DDTS reconstructions using: (a) The curved surface illustrated in Fig. 8 and (b) the flat plane illustrated in Fig. 8(d).

202% is seen between I_T and I_{HC} as random noise is averaged. Both DTS and DDTS show much improved CNR compared to I_T and I_{HC} for the low contrast synthetic calcium, and the further improvement due to the deboning method is clearly seen.

Table 2 and Fig. 10 show the advantage of using a curved, compared to a flat, reconstruction plane, S_{rec} . Table 2 shows the CNR, and change in CNR, when using a curved and flat S_{rec} , and the distance between each piece of synthetic calcium and the flat plane. The distance between the synthetic calcium and the curved reconstruction plane can be assumed to be negligible because the synthetic calcium is attached to the anterior surface of the phantom, and this surface was used as the curved reconstruction S_{rec} . There are only small differences in CNRs for results calculated over PLs 1 and 2 (the two top pieces of synthetic calcium, as shown in Fig. 9(a)) because in this region the flat and curved planes are within 1 mm. However, for the lower piece of synthetic calcium (PL 3), where the flat plane is approximately 10 mm away from the synthetic calcium, a large decrease in CNR (–42%) can be seen. This result is backed up by visual inspection of Fig. 10, where the two top pieces of synthetic calcium look similar, whereas the lower piece of synthetic calcium is blurred in the case of the flat plane (b) compared to the curved plane result (a).

5.2. Patient results

Fig. 11 shows the patient data results. Each row shows a different patient. The columns show: the validation images, I_T (a) and I_{HC} (b); the DTS (c) and DDTS (d) slices; and the CT overlays, aorta outline (e) and calcium (f). In patients 1 and 2 almost no features from the aorta are visible in images I_T and I_{HC} . Whereas in the DTS, and

more so in the DDTS, the aorta outline and some calcium are enhanced, as shown by comparison with the CT overlay images. In patients 3 and 4, which had increased calcium in the aorta, some areas of the aorta outline can be seen in images I_T and I_{HC} . The aorta is most noticeable in regions where the outline does not overly bony anatomy. For patients 3 and 4 the DTS, and again more so for the DDTS, are able to clearly show the aortic outline over most of their length, and are hardly effected by underlying bony features.

It should be noted that the aortic outline visible in the DTS slices is the entire aorta (i.e. patient lumen plus thrombus) whereas in a DSA image only the patient lumen (i.e. where the contrast flows) would be visible. The aortic outline is visible because its linear attenuation coefficient is larger than that of the surrounding connective tissues. Calcium deposits in the aorta increase this difference between linear attenuation coefficients, and so improve visualisation.

5.3. Set-up time and radiation exposure

Time for image acquisition and reconstruction can be split into three main steps:

- The $\sim 20^\circ$ RAO/LAO sweep takes just a few seconds, however, set-up time and explaining the procedure to the radiographer resulted in image acquisition times of up to one minute. This is expected to be reduced greatly if the process became more routine.
- The 2D–3D registration has been optimised to work on GPUs. Registrations performed on a computer with two NVidia GTX 690 graphic cards with each card containing two GPUs took 1.25 s per registration, and so the registration process for all images was around 50 s. The latest graphics cards would reduce this time to approximately 30 s.
- The reconstruction process currently takes between 5 and 10 min. However, this has not yet been optimised, and because relatively simple calculations are required and the process can be highly parallelized, major speed improvements (factors of 100 resulting in 3–6 s reconstruction) are believed possible.

In Table 3 we report the radiation exposure from our DTS sweep, and for comparison the exposure from a mean DSA sequence for patients 2 and 3 (for DTS and DSA acquired with the same field of view). Values were recorded by the fluoroscopy system and saved in the DICOM header as image area dose product (dGy·cm²). DTS radiation exposure for all DTS frames, not just the resampled frames (~ 40), is reported. The table clearly shows that DTS images have a much lower radiation exposure than DSA imaging.

6. Discussion and conclusions

The development of a novel imaging technology capable of soft-tissue visualisation in the interventional suite is challenging. Short acquisition and reconstruction times, low radiation dose and minimal interruption to the clinical work-flow are key requirements

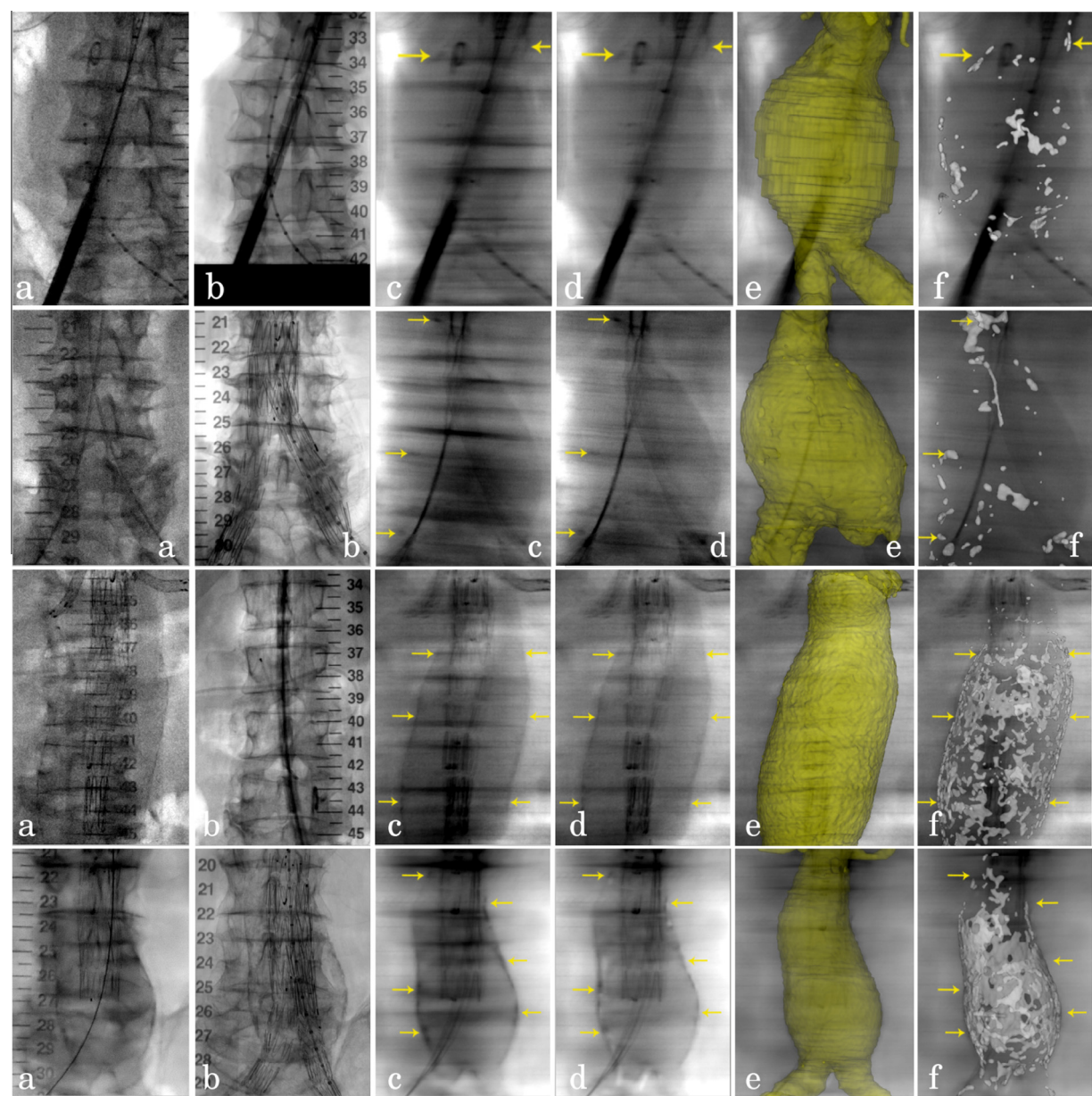


Fig. 11. Patient 1 to patient 4 (top to bottom) results: (a) I_T , (b) I_{HC} , (c) DTS, (d) DDTS, (e) aortic aneurysm overlay and (f) calcification overlay into the DDTS slice. Arrows indicate calcium deposits.

Table 3
Average radiation exposures for the DSA image and DTS sweep for patients 1, 2, and 3.

	DSA (dGy·cm ²)	DTS (dGy·cm ²)
Pat 1: avg. exposure	–	8.65
Pat 2: avg. exposure	120.58	5.03
Pat 3: avg. exposure	93.46	3.68

for an effective interventional modality. At first glance our proposed method appears counter intuitive as we require a high quality CT scan to produce a lower quality DTS slice. However, the high quality CT is already available, and although the DTS is of lower “image” quality, it is far superior in terms of the position of the patient’s anatomy in relation to surgical instruments during the procedure.

We have presented a novel technique, “interventional digital tomosynthesis”, which can be directly implemented on existing

fluoroscopy systems. The small C-arm sweep of $\pm 20^\circ$ took less than one minute for image acquisition. Therefore, disruption to the clinical work-flow was very low compared to cone-beam CT imaging, and is probably equivalent to that of DSA imaging. DSA imaging is routine in endovascular procedures and the greatly increased opacity of the iodinated contrast medium enables much smaller vascular structures to be seen than our proposed DTS method. However, as shown by our patient results (Fig. 11), DTS is able to enhance the aortic outline and calcium deposits; and this can be achieved using no injection of contrast and with a much reduced radiation dose (see Table 3). We propose that DTS could find a role alongside DSA imaging, replacing DSA imaging where appropriate (i.e. observing large scale features such as the aortic outline) while using DSA for critical points in the procedure, and to see small structures.

Our proposed method requires very little set-up and only involves a small angle manual sweep of the C-arm ($\pm 20^\circ$). The

relative positions between each of the 2D sweep images is calculated using 2D–3D registration. Therefore, our method is able to work with any fluoroscopy system, and does not require mechanical tracking of the C-arm or calibration. If information on C-arm position was available then this could be used to speed up the registration process.

A second potential use of DTS imaging is to provide intraoperative information on the position of the aorta to enable non-rigid 2D–3D image registration. As described in Section 4.3 the preoperative CT overlays shown in Fig. 11(e) and (f) needed manual adjustment after the rigid registration to accurately match features of interest in our DDTS images. This was needed to account for aortic deformation caused by the stiff interventional instruments (Carrell et al., 2010). Repeated DTS images could be taken throughout the procedure, which could provide information to a 2D–3D non-rigid registration algorithm (e.g. Guyot et al., 2013) to increase the accuracy of image-guided surgery.

In this work we have concentrated on the use of DTS during interventions, and have designed methods that enable image acquisition and display which fit with the clinical work-flow. The ability to include a preoperative CT scan with the intraoperative imaging has lots of potential to enable more targeted image reconstruction and display. The CT scan can be segmented preoperatively using methods which due to algorithm time, or required amount of manual interaction, would not be appropriate during surgery. Preoperative segmentation of aortic centreline is already part of routine planning for complex EVAR procedures. This then enables intraoperative image reconstruction to automatically extract the clinically useful information. In addition, our proposed method to project reconstructed 3D DTS information back into 2D enables the clinicians to continue operating with their preferred fluoroscopy view, and the process requires no clinician interaction which could interrupt the clinical work-flow.

Intraoperative deformation can occur between the vertebra on which the registration is based and the position of the reconstruction surface. This may cause errors in the position of the reconstruction surface. For a large structure such as the aorta, which is not expected to undergo large deformations (usually less than 10 mm (Carrell et al., 2010)) this is not expected to be a major problem because even after deformation, a reconstruction plane based on preoperative anatomy should still intercept the aorta. However, for visualisation of smaller clinical structures, which move by a larger amount, deformation could result in use of a reconstruction surface a long distance from the intraoperative position of the clinical structure. This would reduce the contrast of the reconstructed clinical structure.

The bone removal process will subtract information segmented from the CT and rigidly registered to the fluoroscopy. We use very simple segmentation process, simply a bounding box around the vertebra and then an intensity threshold. If non-vertebra features are segmented then these will also be subtracted by the method (and so will not be visible in the DTS slice). If these non-vertebra features do not move in a rigid body relationship with the vertebra then artefacts could occur. Further investigations will reveal whether these are important issues. If so, a first step for a solution would be to investigate use of a more sophisticated segmentation algorithm such as Klinder et al., 2009.

The CNR method employed in Section 4.3 was used in a slightly different manner to standard CNR measurement (i.e. a measure of noise reduction). Instead, we used CNR to show how our clinical objects of interest (the aortic wall and synthetic calcium) are more easily detected in our DTS slices due to a reduction of background features and/or artifacts.

Future work is to optimise the image acquisition and reconstruction process and to investigate the potential use of DTS during a series of procedures. The reconstruction process is highly paral-

lelizable and we believe image reconstruction in under a minute is easily achievable on a modern workstation using GPGPU computing. Investigations will be carried out to examine the effect on image quality and clinical acceptability (patient dose and interruption to work-flow) when varying image acquisition: C-arm sweep range and frame rate. Clinicians will be able to view the DTS slices during the procedure, and we will investigate the image quality of desired clinical features and potential of DTS to aid guidance.

In summary, a novel method for interventional DTS has been presented. The method employs a 2D–3D registration algorithm to enable production of DTS slices using standard interventional equipment, with much reduced out-of-plane clutter, and on a patient tailored reconstruction surface. Results from a phantom and four patients show the method's ability to automatically enhance structures of clinical interest.

References

- Bachar, G., Barker, E., Nithianathan, S., Chan, H., Daly, M., Irish, J., Siewerdsen, J., 2009. Three-dimensional tomosynthesis and cone-beam computed tomography: an experimental study for fast, low-dose intraoperative imaging technology for guidance of sinus and skull base surgery. *The Laryngoscope* 119, 434–441.
- Bachar, G., Siewerdsen, J., Daly, M., Jaffray, D., Irish, J., 2007. Image quality and localization accuracy in C-arm tomosynthesis-guided head and neck surgery. *Med. Phys.* 34, 4664.
- Carrell, T., Modarai, B., Brown, J., Penney, G., 2010. Feasibility and limitations of an automated 2D–3D rigid image registration system for complex endovascular aortic procedures. *J. Endovasc. Ther.* 17, 527–533.
- Demirci, S., Manstad-Hulaas, F., Navab, N., 2009. Quantification of abdominal aortic deformation after EVAR. In: *SPIE Medical Imaging, International Society for Optics and Photonics*, pp. 72611U–72611U.
- Dobbins III, J., McAdams, H., 2009. Chest tomosynthesis: technical principles and clinical update. *Eur. J. Radiol.* 72, 244–251.
- Dobbins III, J., 2009. Tomosynthesis imaging: at a translational crossroads. *Med. Phys.* 36, 1956–1967.
- Dobbins III, J., Godfrey, D., 2003. Digital X-ray tomosynthesis: current state of the art and clinical potential. *Phys. Med. Biol.* 48, 65–106.
- Dobbins III, J.T., McAdams, H.P., Song, J.W., Li, C.M., Godfrey, D.J., DeLong, D.M., Paik, S.H., Martinez-Jimenez, S., 2008. Digital tomosynthesis of the chest for lung nodule detection: interim sensitivity results from an ongoing NIH-sponsored trial. *Med. Phys.* 35, 2554–2557.
- Gang, G., Tward, D., Lee, J., Siewerdsen, J., 2010. Anatomical background and generalized detectability in tomosynthesis and cone-beam CT. *Med. Phys.* 37.
- Guyot, A., Varnavas, A., Carrell, T., Penney, G., 2013. Non-rigid 2D–3D registration using anisotropic error ellipsoids to account for projection uncertainties during aortic surgery. In: *Medical Image Computing and Computer-Assisted Intervention – MICCAI 2013*. Springer, pp. 179–186.
- Jaffray, D., Siewerdsen, J., Wong, J., Martinez, A., et al., 2002. Flat-panel cone-beam computed tomography for image-guided radiation therapy. *Int. J. Radiat. Oncol. Biol. Phys.* 53, 1337–1349.
- Klinder, T., Ostermann, J., Ehm, M., Franz, A., Kneser, R., Lorenz, C., 2009. Automated model-based vertebra detection, identification, and segmentation in CT images. *Med. Image Anal.* 13, 471–482.
- Levakhina, Y., Müller, J., Duschka, R., Vogt, F., Barkhausen, J., Buzug, T., 2013. Weighted simultaneous algebraic reconstruction technique for tomosynthesis imaging of objects with high-attenuation features. *Med. Phys.* 40, 031106.
- Markelj, P., Tomaževič, D., Likar, B., Pernuš, F., 2012. A review of 3D/2D registration methods for image-guided interventions. *Med. Image Anal.* 16, 642–661.
- McCullough, P.A., 2008. Contrast-induced acute kidney injury. *J. Am. Coll. Cardiol.* 51, 1419–1428.
- Orth, R., Wallace, M., Kuo, M., 2008. C-arm cone-beam CT: general principles and technical considerations for use in interventional radiology. *J. Vasc. Interv. Radiol.* 19, 814–820.
- Penney, G., Varnavas, A., Dastur, N., Carrell, T., 2011. An image-guided surgery system to aid endovascular treatment of complex aortic aneurysms: description and initial clinical experience. In: *IPCAI*, vol. 6689, pp. 13–24.
- Penney, G., Weese, J., Little, J., Desmedt, P., Hill, D., et al., 1998. A comparison of similarity measures for use in 2D/3D medical image registration. *IEEE. Trans. Med. Imaging* 17, 586–595.
- Seeliger, E., Sendeski, M., Rihal, C., Persson, P., 2012. Contrast-induced kidney injury: mechanisms, risk factors, and prevention. *Eur. Heart J.* 33, 2007–2015.
- Siewerdsen, J., Daly, M., Bachar, G., Moseley, D., Bootsma, G., Brock, K., Ansell, S., Wilson, G., Chhabra, S., Jaffray, D., et al., 2007. Multimode C-arm fluoroscopy, tomosynthesis, and cone-beam CT for image-guided interventions: from proof of principle to patient protocols. In: *SPIE Med Imaging*, pp. 65101A–65101A.
- Skaane, P., Gullien, R., Bjørndal, H., Eben, E.B., Ekseth, U., Haakenaasen, U., Jahr, G., Jebens, I.N., Krager, M., 2012. Digital breast tomosynthesis (DBT): initial experience in a clinical setting. *Acta Radiol.* 53, 524–529.

- Teertstra, H.J., Loo, C.E., van den Bosch, M.A., van Tinteren, H., Rutgers, E.J., Muller, S.H., Gilhuijs, K.G., 2010. Breast tomosynthesis in clinical practice: initial results. *Eur. Radiol.* 20, 16–24.
- Tingberg, A., 2010. X-ray tomosynthesis: a review of its use for breast and chest imaging. *Radiat. Prot. Dosim.* 139, 100–107.
- Wallace, M., Kuo, M., Glaiberman, C., Binkert, C., Orth, R., Soulez, G., 2008. Three-dimensional C-arm cone-beam CT: applications in the interventional suite. *J. Vasc. Interv. Radiol.* 19, 799–813.
- Weese, J., Penney, G.P., Desmedt, P., Buzug, T.M., Hill, D.L., Hawkes, D.J., 1997. Voxel-based 2-D/3-D registration of fluoroscopy images and CT scans for image-guided surgery. *IEEE Trans. Inf. Technol. Biomed.* 1, 284–293.
- Yushkevich, P.A., Piven, J., Hazlett, H.C., Smith, R.G., Ho, S., Gee, J.C., Gerig, G., 2006. User-guided 3D active contour segmentation of anatomical structures: significantly improved efficiency and reliability. *Neuroimage* 31, 1116–1128.